Powder flow down a vertical pipe: the effect of air flow

By Y. BERTHO[1], F. GIORGIUTTI-DAUPHINÉ[1],
T. RAAFAT[1,2], E. J. HINCH[3], H. J. HERRMANN[2]
AND J. P. HULIN[1]

[1]Laboratoire FAST, UMR 7608, Bat. 502, Campus Universitaire, 91405 Orsay Cedex, France
[2]Laboratoire PMMH, ESPCI, UMR 7636, 10 rue Vauquelin, 75231 Paris, Cedex 05, France
[3]Department of Applied Mathematics and Theoretical Physics, University of Cambridge,
Silver Street, Cambridge CB3 9EW, UK

The dynamics of dry granular flows down a vertical glass pipe of small diameter have been studied experimentally. Simultaneous measurements of pressure profiles, air and grain flow rates and volume fractions of particles have been realized together with spatio-temporal diagrams of the grain distribution down the tube. At large grain flow rates, one observes a stationary flow characterized by high particle velocities, low particle fractions and a downflow of air resulting in an underpressure in the upper part of the pipe. A simple model assuming a free fall of the particles slowed down by air friction and taking into account finite particle fraction effects through Richardson–Zaki's law has been developed: it reproduces pressure and particle fraction variations with distance and estimates friction forces with the wall. At lower flow rates, sequences of high-density plugs separated by low-density bubbles moving down at a constant velocity are observed. The pressure is larger than outside the tube and its gradient reflects closely the weight of the grains. Writing mass and momentum conservation equations for the air and for the grains allows one to estimate the wall friction, which is less than 10% of the weight for grains with a clean smooth surface but up to 30% for grains with a rougher surface. At lower flow rates, oscillating-wave regimes resulting in large pressure fluctuations are observed and their frequency is predicted.

1. Introduction

Dry granular media are at present a very active domain of research both because of their fundamental interest in relation to the modelling of disordered and dispersed media and because of their many areas of practical application. Granular media are encountered in many areas such as the food industry, and civil and chemical engineering (Jaeger & Nagel 1992; Duran 1997; Behringer & Jenkins 1997). A particularly important problem is the flow of these materials in pipes and channels (Jackson 2000).

A first type of study deals with systems in which the interaction between the flowing grains and air is negligible (Savage 1979). These flows frequently undergo instabilities (Wang, Jackson & Sundaresan 1997) and density waves may then appear. Such waves were for instance observed experimentally between parallel walls by Reydellet, Rioual & Clement (2000) and can be reproduced by numerical simulations using molecular dynamics (Pöschel 1994; Lee 1994) or lattice-gas methods (Peng & Herrmann 1994).

Analysis in terms of kinetic wave theories can be applied to these phenomena (Leibig 1994; Lee & Leibig 1994) which bear strong similarities with density waves in traffic flows (Lighthill & Whitham 1955; Musha & Higuichi 1976).

In most cases of interest, however, the interaction of the air with the flowing grains plays a key part. This is particularly the case in practical applications to pneumatic transport, catalytic cracking, fluid beds and emptying storage silos. Very diverse flow regimes such as moving packed particle beds, fluidized suspensions and combinations of these regimes are observed in these systems (Leung & Jones 1978). These regimes may coexist in a flow system, particularly when gas is injected locally into the flow pipe (Mountziaris & Jackson 1990). Furthermore, these flows may display unwanted intermittency, oscillations and/or blockages: a periodic intermittent flow of this type is observed in 'ticking hourglass' experiments as grains flow through a constriction connecting two glass reservoirs (Le Pennec *et al.* 1995, 1996, 1998). This effect again results from interactions between the interstitial air and the grains.

Very detailed and elaborate theoretical models have been developed to analyse these flows and take into account the interaction between air and the grains (Leung & Jones 1978; Ginestra, Rangachari & Jackson 1980; Chen, Rangachari & Jackson 1984; Sinclair & Jackson 1989; Nott & Jackson 1992; Jackson 2000). These models predict flow configurations and characteristic parameters in the different parts of the flow from a small number of input variables (the grain flow rate for instance). When experiments are available, the predictions of these theoretical models are generally checked against pressure profile measurements Chen *et al.* (1984); other parameters are estimated theoretically. More recent experimental work has included a larger number of measurements, allowing one in particular to analyse the particle distribution in the flow channels (Srivastava *et al.* 1998). Although the above approach is very well suited to modelling complete large systems, it requires the introduction of a large number of relations between the various variables, based on published literature and on experimental or empirical correlations. This may result in significant uncertainties in the values of key variables.

In the present work we used a different approach and performed a set of experiments on a very simple flow system (a plain vertical glass tube with a feeding hopper at the top and a variable constriction at the bottom) equipped with a large number of sensors. They allowed us to determine simultaneously the grain and air flow rates, the local solid volume fraction at two positions along the tube and the pressure profile. In addition, a linear camera gives spatio-temporal diagrams of the grain distribution along the tube allowing a detailed analysis of the dynamical properties of the flow. In this way, many variables are directly measured instead of needing to be estimated through theoretical or empirical relations. Relatively simple theoretical developments are then needed since most other parameters of interest can generally be determined reliably through simple conservation equations: friction forces on the pipe wall can in particular be estimated simply.

Using a simple set-up also allows us to explore systematically a broad range of control parameter values: as shown in previous papers (Raafat, Hulin & Herrmann 1996; Aider *et al.* 1999), it is possible to observe a large variety of flow regimes by varying the grain flow rate. We observe in particular, at intermediate grain flow rates, density waves in which compact plugs are separated by bubbles with a low volume fraction of particles (the volume fraction of particles will in the following be called the 'particle fraction'). The plugs move generally at constant velocity but may display oscillations in a few cases. At higher flow rates, a low-particle-fraction high-velocity free-fall regime is observed. At lower flow rates, the grain flow may be

stationary or intermittent and is characterized by a low velocity and a high particle fraction ($\approx 60\%$): this latter regime is similar to the flows of particle beds discussed by Ginestra *et al.* (1980). Its properties, and particularly the intermittency associated with it, will be reported in a subsequent work and the present paper deals with the two other regimes in the case of vertical tubes. As stated in the introduction, other flow regimes can appear in such systems such as the coexistence of a free fall and a compact regime (Mountziaris & Jackson 1990) but they were not observed in the present work.

After describing the experimental procedure, the high-velocity free-fall regime will be first studied experimentally and analysed theoretically: it will be shown that both the pressure and the particle fraction profiles can be reproduced quantitatively by a simple set of equations and that the friction force on the walls can be determined reliably. A similar approach will be used to study the pressure distribution and the wall friction in the constant-velocity wave regime, with particular attention given to the dependence of wall friction on the roughness of the grain surface. The same approach is, finally, extended to an oscillating-wave regime in which analogies with sound propagation in two-phase flows appear.

2. Experimental procedure

2.1. *Experimental set-up*

In the present work, we study the flow of glass beads of diameter $2a = 175 \pm 25\,\mu m$ and of density $\rho_g = (2.5 \pm 0.02)10^3\,kg\,m^{-3}$ (the glass density is measured by comparing the weight of a picnometer of precisely known volume filled first with water and then with a known mass of beads saturated with water). The experimental flow channel (figure 1*a*) is a vertical glass pipe of length $L = 1.25\,m$ and of internal diameter $2R = 3 \pm 0.05\,mm$ welded to the bottom of a spherical hopper. The bottom end of the pipe is fitted with a variable constriction allowing one to adjust the outflow. Computer-controlled scales placed below the tube monitor the mass of grains flowing out at the bottom end. The mass flow rate Q_m is then determined by differentiation with respect to time. In the following the grain flow rate is characterized by the superficial velocity q (i.e. the volume flow rate of the grains per unit area) with

$$q = \frac{Q_m}{\pi R^2 \rho_g} \tag{1}$$

The hopper is a container with one opening at its bottom serving as a connection to the experimental tube and a side inlet allowing an inflow of air monitored by a Honeywell gas flow rate sensor. The measurement ranges are $1\,l\,mn^{-1}$ or $4\,l\,mn^{-1}$ and the sensors are calibrated by means of a variable-flow-rate displacement syringe pump; the volume flow rate Q_{meas} of inflowing air is measured in this way with a precision of $\pm 1\%$. As for grains, the flow of air through the tube is characterized by a superficial velocity q_a (i.e. the volume flow rate per unit area in the experimental tube section). Note that q_a is not equal to $Q_{meas}/\pi R^2$ but that

$$q_a = \frac{1}{\pi R^2}\left(Q_{meas} - \frac{Q_m}{\rho_g}\right) = \frac{Q_{meas}}{\pi R^2} - q. \tag{2}$$

The inflow of air must compensate both the volume flow rate Q_m/ρ_g of the grains which flow out of the hopper and that of the air which flows out of the hopper into the tube.
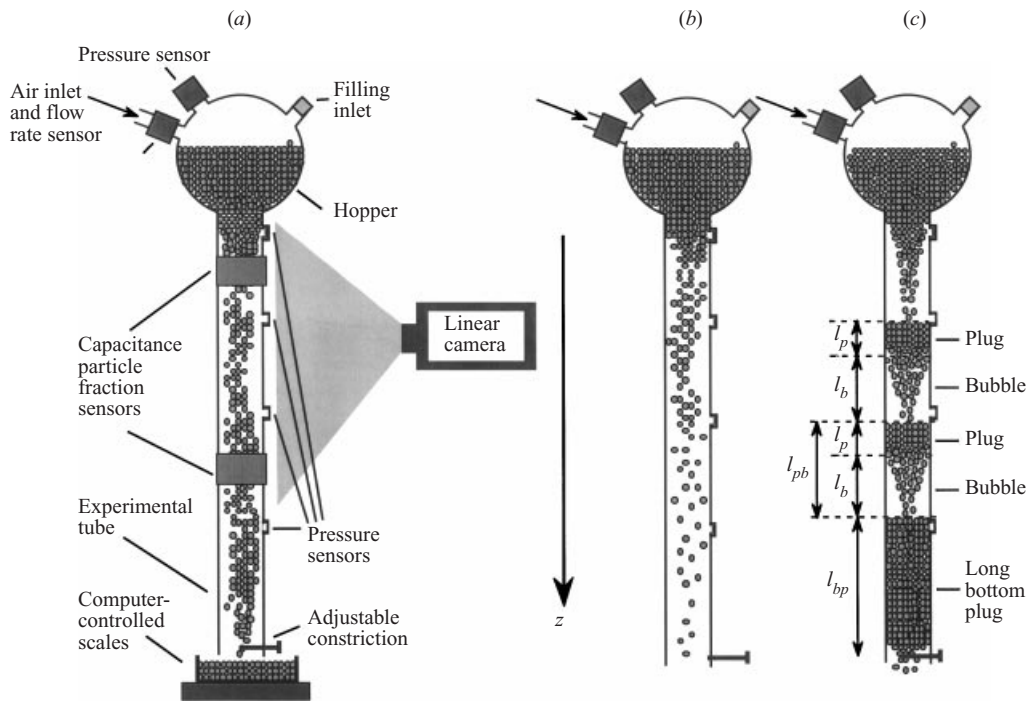
FIGURE 1. (*a*) Experimental set-up for vertical granular flow studies. (*b*) Schematic view of the free-fall regime. (*c*) Schematic view of the density-wave regime.

Pressure variations along the pipe are monitored by four sensors located along the tube at vertical distances of 200, 450, 700 and 950 mm below the outlet of the hopper. We use solid-state strain-gauge sensors attached directly to the tube wall with a measurement range of 3×10^4 Pa, a resolution of the order of 100 Pa and a response time of a few 10^{-2} s: the transducers have a low internal volume of a few mm^3 and are connected by short (5 mm long), 1 mm ID tubes to 0.5 mm diameter holes in the experimental pipe. A fine-meshed grid is stretched across them in order to avoid grains penetrating the sensors. Another transducer measures pressure in the hopper.

Variations of the mean particle fraction in a tube section are estimated from the measurement of the electrical capacitance between two 3 mm diameter cylindrical electrodes with their ends against the outside tube wall and facing each other. Careful shielding reduces the global capacitance of the probe to a few 10^{-2} pF and the electrode assembly can be moved along the tube. Using a General Radio 1615A capacitance bridge and a lock-in detector with a 3 ms time constant and a 10 kHz measurement frequency gives a very good measurement stability and a noise level equivalent to a few 10^{-5} pF. The DC output is assumed to vary roughly linearly with the particle fraction since the corresponding capacitance variations are only a minor fraction of the global value; the measurement is then calibrated by comparing readings obtained with an empty tube and with the same tube containing a bead packing of particle fraction 63% (estimated by weighing the grains and independently measuring their density). The noise level corresponds to particle fraction variations of order 0.5%. We estimate the vertical resolution of the measurement by moving the upper boundary of the grain packing in a partly filled tube through the sensor

and recording the output reading for each location: the corresponding capacitance variation is roughly linear and spreads over 2 mm which therefore represents the typical spatial resolution of the measurement.

A Spectral Dynamics SD195 signal analyser records instantaneous variations of the readings of four sensors (up to a 200 kHz sampling frequency), while averages of 10 physical parameters over time intervals of 1 s are recorded simultaneously.

Another important issue is the determination of the various characteristic velocities of the flow. Mean air and grain velocities can be estimated by combining grain and air flow rate values with those of the particle fraction; on the other hand the velocity of the plugs in the wave regime can be determined from spatio-temporal diagrams of the particle density distribution along the pipe. Such diagrams were also constructed for the free-fall regime and provide the velocity of small density fluctuations associated with small aggregates of particles. Spatio-temporal diagrams are obtained by means of a digital linear CCD camera mounted on a micrometric assembly allowing a precise alignment of the view field of the camera with the flow tube. The readings of all the pixels of the linear sensor are directly transmitted to a computer at a repetition rate of 2000 Hz for the free-fall regime and 500 Hz for the wave regime. Spatio-temporal diagrams obtained in this way are stored as numerical data arrays which can be visualized by standard image processing programs; in addition they allow one to detect with great sensitivity oscillations and intermittencies of the flow and to measure the propagation velocity of the perturbations.

2.2. *Flow regime dependence on granular flow rate and humidity*

The key parameter determining the flow regime is the granular flow rate, but the degree of humidity H of the ambient air also significantly influences the flow regimes observed. Breathing into the pipe for a second generates enough humidity on the walls to completely block the flow of grains in the tube. More generally, large values of humidity often induce clogging due to capillary forces between particles or between particles and tube walls. On the other hand, if the atmosphere is too dry, electrostatic forces appear and may also lead to a blocking of the flow. Humidity is monitored by an electronic hygrometer and adjusted by a humidifier in order to obtain a good reproducibility during a series of experimental runs.

The free-fall regime characterized by high velocities and low densities of particles is only observed for grain flow rates with $q > 0.35 \,\mathrm{m\,s^{-1}}$ with little or no constriction at the bottom (figure 1*b*). When the constriction is increased, the flow switches to a regime with density waves of constant velocity in the range of flow rates $0.11 < q < 0.26 \,\mathrm{m\,s^{-1}}$ (and for relative humidities between 45% and 55%). In this case, a system of high-density plugs and low-density bubbles moves at a constant downward velocity (figure 1*c*). For narrower constrictions and q of order 0.085–0.11 $\mathrm{m\,s^{-1}}$, the waves may start to oscillate with a system of plugs and bubbles moving up and down with an amplitude of the order of a centimetre: this is particularly the case at low humidity. At still lower flow rates $q < 0.08 \,\mathrm{m\,s^{-1}}$, a compact flow is observed with a slow constant velocity or an intermittent motion of the particles. This regime, in which solid contact forces play a crucial role, will be discussed in a future paper and we shall deal here only with free-fall and wave regimes.

In order to demonstrate qualitatively the influence of the contact forces in the wave regime, we report near the end of the paper (§5) a few experiments realized with beads which had been processed many times through the experimental tube and had their surface roughened by collisions with the walls and with each other.
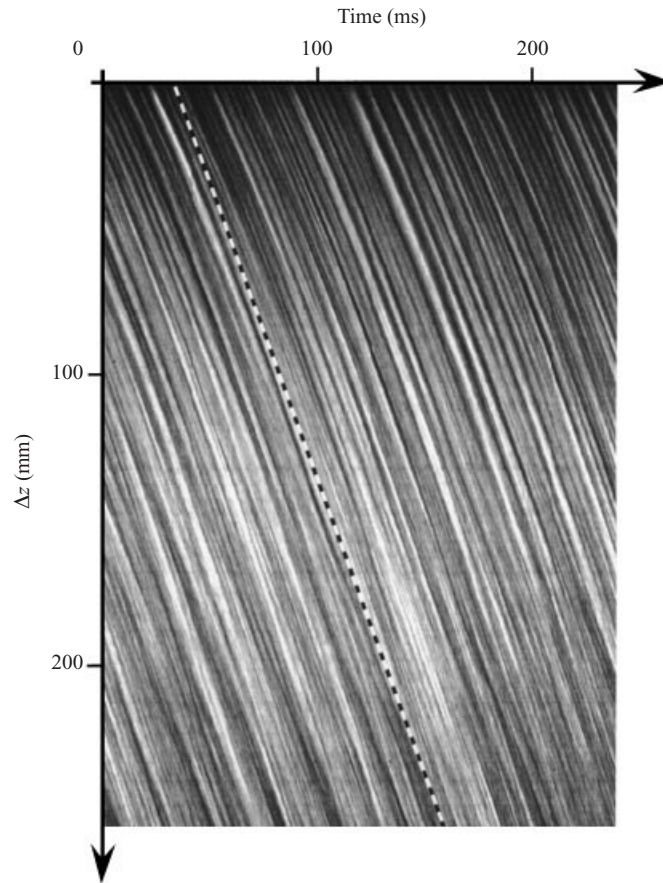
FIGURE 2. Spatio-temporal images of the fluctuations of particle distribution along the flow tube obtained with a linear camera in the free-fall regime. The dashed line corresponds to a constant velocity of $2.3\,\mathrm{m\,s^{-1}}$. Line sampling rate: $2000\,\mathrm{Hz}$, height of field of view: $256\,\mathrm{mm}$, duration of recording: $240\,\mathrm{ms}$, Δz is the distance from the top of the tube.

Otherwise, all experimental results presented here correspond to beads used in only a few experiments and displaying a smooth surface.

3. Stationary free-fall regime

3.1. *Experimental observations*

In this regime, a fast flow of the particles is observed, with no apparent velocity fluctuations (no detectable flow rate variation is observed by measuring the mass of grains flowing out of the tube either). Pressure fluctuations measured on the local transducers are also of very small amplitude (1–2% of the average value) confirming the near stationary nature of the flow. The superficial velocity of the grains (typically $q = 0.35–0.55\,\mathrm{m\,s^{-1}}$) is large and associated with a large downward air flow ($q_a = 2–3\,\mathrm{m\,s^{-1}}$). This regime can be compared to the flow of suspensions (Leung & Jones 1978; Chen *et al.* 1984) down a standpipe: the superficial velocities of the grains are similar (even though the pipe diameter is ten times smaller in our work) but the particle fraction is estimated to be of the order of 60% (instead of around 20% in our experiments). Since this free-fall flow regime is stationary and the
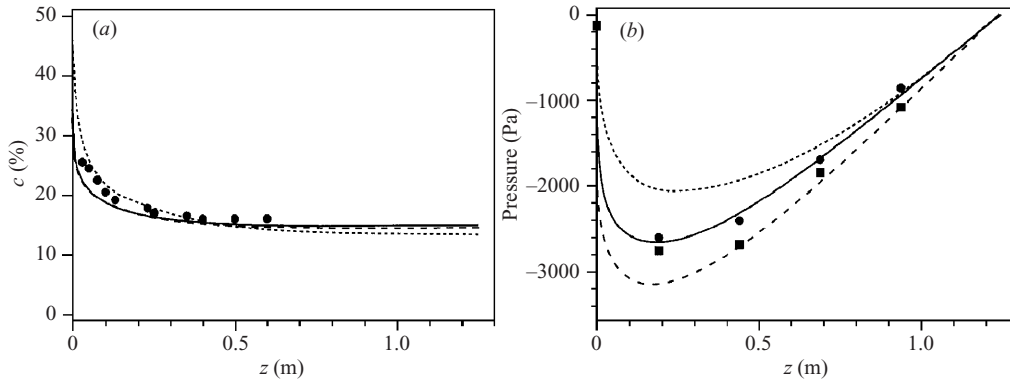
FIGURE 3. (*a*) Particle fraction variations in a free-fall flow along a 1.25 m long tube as a function of the distance z from the top of the tube for a grain flow rate $q = 0.56 \, \text{m s}^{-1}$. ●, experimental values. Lines correspond to theoretical predictions under different assumptions: -----, friction force on particles given by the Stokes formula; – –, Friction force corrected for finite Reynolds number and finite particle fraction effects and wall friction force F_w equal to zero; ——, Friction force corrected for finite Reynolds number and particle fraction effects and wall friction force F_w equal to 15% of grain weight. (*b*) Time-averaged relative pressures with respect to atmosphere at four different distances z. ●, $q = 0.56 \, \text{m s}^{-1}$; ■, $q = 0.54 \, \text{m s}^{-1}$ (the atmospheric pressure p_{at} is taken equal to zero). Lines correspond to theoretical predictions for $q = 0.56 \, \text{m s}^{-1}$ under the same asssumptions in 3(*a*).

characteristic parameters vary slowly along the tube, it represents a suitable case to test our measurements against a simple theoretical model of the flow.

Spatio-temporal diagrams of the density fluctuations along the tube (figure 2) display parallel striations reflecting the motion of small grain clusters and/or of local density fluctuations (the spatial resolution, typically 1 mm, is not good enough to detect the motion of individual grains). The lines are slightly curved at the upper part of the tube (reflecting the flow acceleration) and reach a constant slope (dashed line in figure 2) at a typical distance of 0.5 m below the hopper: this slope corresponds to a large constant velocity v_∞ of order 2.3 m s^{-1}.

These qualitative observations can be compared to the particle fraction profiles $c(z)$ along the tube: the particle fraction decreases quickly (figure 3a) and reaches a limiting value c_∞ of order 0.16 at about 0.5 m below the top. This is accompanied by an increase of the grain velocity $v(z)$ with distance since the superficial velocities q and q_a satisfy (assuming a steady state):

$$q = c(z)v(z), \tag{3}$$

$$q_a = (1 - c(z))v_a(z). \tag{4}$$

The low value of c_∞ gives a large difference between the superficial velocity q and the limit velocity v_∞. The increase of $v(z)$ is in qualitative agreement with the spatio-temporal diagram of figure 2. Equation (4) indicates that air velocity must, on the other hand, decrease with distance. The flows of grain and air induce, in turn, pressure variations displayed as a function of z in figure 3(*b*) for different velocities $0.45 < q < 0.55 \, \text{m s}^{-1}$ (the atmospheric pressure p_{at} will be taken equal to zero in the following). A large underpressure region (3000 Pa lower) appears in the upper part of the tube, while in the region $z > 0.5$ m where $c(z)$ has reached its limiting value, pressure increases linearly until it reaches atmospheric pressure ($p_{at} = 0$) at the outlet. The point at $z = 0$ represents the pressure measured in the hopper above the grain

packing and is very close to zero: a strong pressure gradient above $z = 0.2\,\text{m}$ results, which explains the large downward air flow through the porous grain packing.

Let us now write the equations of motion for the air and for the grains (Ginestra *et al.* 1980; Chen *et al.* 1984): combined with the mass conservation equations above they will allow us to determine friction forces on the walls from pressure and particle fraction profiles without needing further relations. Assuming in addition a simple expression from the literature for the friction force between air and the grains, it will then be possible to predict the full pressure and particle fraction profiles along the pipe for given flow rates q and q_a.

3.2. *Equations of motion for the air and for the grains and estimates of friction forces*

It is assumed here that the flow is stationary in time and homogeneous across a given section of the tube. Then, the velocities v_a and v of air and of the grains respectively depend only on the distance z from the bottom of the hopper (taken positively downwards) and are related to the particle fraction $c(z)$ by equations (3) and (4). Let us first assume that the friction force between the grains and the tube walls is negligible. Then, when the flow is stationary, the Lagrangian acceleration $dv(z)/dt = v(z)\,dv(z)/dz$ satisfies

$$mv(z)\frac{dv(z)}{dz} = mg - F(v(z) - v_a(z)). \tag{5}$$

Here m is the mass of a single grain given by $m = 4\pi\rho_g a^3/3$ and $F(v(z) - v_a(z))$ is the friction force on the grain, which depends only on the relative velocity of the particles with respect to the air. On the other hand, the equation of motion of air can be reduced to

$$\frac{dp}{dz} = \rho_g c(z)\frac{F(v(z) - v_a(z))}{m}, \tag{6}$$

in which $\rho_g c(z)/m$ is equal to the number of particles per unit volume. Equation (6) assumes a balance between the pressure gradient and the friction force between the air and the grains: this amounts to neglecting both the Lagrangian acceleration $\rho_a v(z)\,dv(z)/dz$ and the friction force of air on the walls. The first term is negligible due to the low density of air and the second is shown below to be markedly smaller than the pressure gradient. Equation (6) may be combined with (5) to obtain the following equation which does not include explicitly the friction force F:

$$\frac{dp}{dz} = \rho_g g c(z) - \rho_g c(z)v(z)\frac{dv(z)}{dz}. \tag{7}$$

At large enough distances from the hopper ($z > 0.4\,\text{m}$), the particle fraction $c(z)$ and the velocities v and v_a reach the limiting values $c_\infty = 0.16$, v_∞ and $v_{a\infty}$ (figure 3), and the term $\rho_g c(z)v(z)\,dv(z)/dz$ is equal to zero in (7). However the value of (dp/dz) predicted by taking $c_\infty = 0.16$ in (7) is of the order of $3900\,\text{Pa}\,\text{m}^{-1}$ which is larger than the experimental value $(dp/dz) = 3500\,\text{Pa}\,\text{m}^{-1}$ at long distances (figure 3). This difference implies that the friction force on the walls is not zero and that (7) must be replaced (in the constant-pressure-gradient and velocity region) by

$$\frac{dp(z)}{dz} = \rho_g g c_\infty - \frac{F_w}{\pi R^2}. \tag{8}$$

F_w is the friction force on the walls per unit length of the tube and is of the order of 15% of the grain weight for $q = 0.56\,\text{m}\,\text{s}^{-1}$ (as in figure 3*a*). Let us show now that F_w is made up mostly of the friction force F_{wg} between grains and the walls and that the

component F_{wa} due to air friction with the walls is negligible. Estimating F_{wa} is not straightforward since the flow profile is strongly influenced by the grains (estimating the frictional force between the grains and the walls would be even more difficult). The typical Reynolds number Re of the global air flow in the tube defined as $2Rv_m/v$ is of order 400 (for a mean air velocity v_m of the order of the limiting velocity $3\,\mathrm{m\,s^{-1}}$). An upper bound on the pressure drop component due to air friction with the walls may be obtained by considering a characteristic roughness ε of the tube walls of the order of the grain radius a. A classical (Olson 1970) approximate expression for the characteristic friction velocity u^* is given by the relation:

$$\frac{u}{u^*} = 2.5\ln(r/\varepsilon) + 8.5,$$

where r is the radial position in the pipe. After integration, one obtains

$$u^* = \frac{v_m}{2.5\ln(R/\varepsilon) + 7.25}.$$

With the values of the physical parameters given above, one obtains $u^* \approx 0.2\,\mathrm{m\,s^{-1}}$ and $v_m \approx 3\,\mathrm{m\,s^{-1}}$, which corresponds to the following pressure gradient:

$$\left|\frac{\partial p}{\partial z}\right| = \frac{f}{D}\rho_a \frac{v_m^2}{2}, \tag{9}$$

where f is a friction factor which depends on the Reynolds number and the rugosity and is of the order of 0.06. Thus, one finds $|\partial p/\partial z| \approx 110\,\mathrm{Pa\,m^{-1}}$. This justifies the assumption that this contribution to the pressure gradient term is negligible.

3.3. *Computation of theoretical pressure and particle fraction profiles and comparison with experimental results*

In order to determine the profiles $p(z)$ and $c(z)$, one first needs to compute the friction force $F(v(z) - v_a(z))$. At the relative velocities of the particles with respect to the air found in our experiments ($3\,\mathrm{m\,s^{-1}}$ at most), the corresponding Reynolds number $Re_a = 2a(v - v_a)/v$ (v being the kinematic viscosity of air), is always below 100 at low concentrations. Then, in the low particle concentration limit, the force F may be approximated by the empirical relation (Olson 1970)

$$F(v - v_a) = 6\pi\eta a(v - v_a)\left(1 + \tfrac{3}{16}Re_a\right)^{1/2} \tag{10a}$$

(η is the dynamic viscosity of air), which reduces at very low Reynolds numbers to the classical Stokes relation. In our experimental case, the dilute approximation is not valid since measured particle fractions range between 15% and 25% and the particle fraction is still higher at the upper end of the tube. We take into account these finite concentrations by introducing a correction factor estimated from Richardson & Zaki's (1954) classical relation between the sedimentation velocity $v_s(c)$ of a suspension and the Stokes settling velocity for a single isolated particle v_{stokes}. This equation is written as $v_s(c) = v_{stokes}(1 - c)^n$ in which the exponent n is taken equal to 5.5 at low Reynolds numbers: this implies that the coefficient $6\pi\eta a$ in equation (10a) must be multiplied by $(1 - c)^{n-1}$ (the additional factor $1/(1 - c)$ reflects the fact that sedimenting particles induce a backflow of the suspending fluid so that the relative velocity is actually $v_s(c)/(1 - c)$). Equation (10a) then becomes

$$F(v - v_a) = 6\pi\eta a(v - v_a)\left(1 + \tfrac{3}{16}Re_a\right)^{1/2}\frac{1}{(1 - c)^{n-1}}. \tag{10b}$$

Combining equations (3)–(5) and (10b), one obtains the following first-order differential equation for $c(z)$ (assuming at this stage $F_w = 0$):

$$\frac{\mathrm{d}c}{\mathrm{d}z} = -g\frac{c^3}{q^2} + \frac{6\pi\eta ac^3}{mq^2}\left(\frac{q}{c} - \frac{q_a}{1-c}\right)\left[1 + \frac{3}{8}\frac{a}{v}\left(\frac{q}{c} - \frac{q_a}{1-c}\right)\right]^{1/2}\frac{1}{(1-c)^{n-1}}, \quad (11a)$$

which, for low Reynolds numbers and low particle fractions, becomes

$$\frac{\mathrm{d}c}{\mathrm{d}z} = -g\frac{c^3}{q^2} + \frac{6\pi\eta a}{m}\left(\frac{c^2}{q} - \frac{c^3 q_a}{q^2(1-c)}\right). \quad (11b)$$

Equations (11a) and (11b) are then integrated numerically to obtain the theoretical particle fraction profiles $c(z)$ displayed in figure 3(a). Note that the value $c(0)$ right at the top of the hopper cannot be determined precisely due to the fast variation of $c(z)$ in this region: on the other hand (and for the same reason) the choice of $c(0)$ does not markedly influence $c(z)$ in regions of slower variation farther from the hopper. Even a large variation of $c(0)$ corresponds to an uncertainty of a few mm in the z scale of the profiles, which has a small influence on the value of $c(z)$, except very close to the hopper. We have chosen the value $c = 0.5$, which is a good order-of-magnitude estimate of the particle fraction just after decompaction, to obtain the curves of figure 3(a). In order to determine $c(z)$, we have used in (11a, b) the experimental value of the air flow q_a. This air flow might alternatively be estimated for a given grain flow q from the permeability and particle fraction of the grain packing in the hopper and the pressure variation across this packing. This estimate would however be much less precise than the direct measurement in view of the uncertainty in these parameters.

One observes first in figure 3(a) that the fit of the theoretical curves with the experimental data is improved by including finite Reynolds number and particle fraction effects. The theoretical profiles also confirm the experimental observation that $c(z)$ reaches a lower limit c_∞ at a distance of 0.4 m. This limiting value c_∞ is equal to 0.14 when the friction force F_w is omitted. In order to obtain the experimental value 0.16, a friction force F_w equal to 15% of the grain weight must be introduced, as already found in the previous section (this amounts to decreasing the gravity acceleration g by 15%). The third curve in figure 3(a) corresponds to this hypothesis and differs little near the hopper from that corresponding to $F_w = 0$, while the fit becomes better further down the tube. Note that the value 0.15 of the ratio between F_w and the grain weight can be determined directly from (7) and does not depend on the expression for the friction force F between the air and the grains. This ratio should depend however on various flow parameters such as the flow rate, the surface condition of the grains and of the tube and their diameters. Similar observations have been reported on pressure gradients in circulating fluidized beds (although at higher particle fractions) by Srivastava *et al.* (1998) and were also interpreted in terms of wall friction.

Theoretical pressure profiles $p(z)$ are computed at the same time as $c(z)$ by means of (6) (at each step of the integration, the friction force F is computed by combining equations (3), (4) and (11a, b)). The integration constant is then chosen to give the atmospheric pressure at the lower outlet of the tube. Closer to the top of the tube, the fit between experimental and theoretical pressure variations is markedly better when the effects of the finite Reynolds number and particle fraction values are taken into account (figure 3b); it is further improved by introducing the friction force F_w of the grains with the walls.
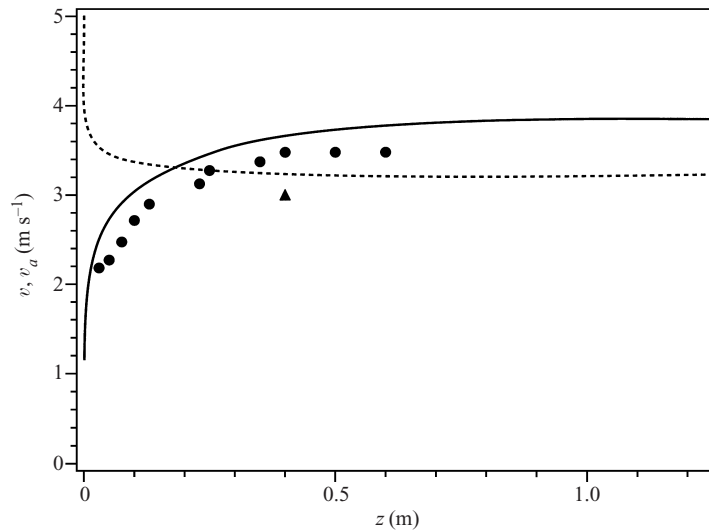
FIGURE 4. Air and grain velocity variations in a free-fall flow ($q = 0.56 \, \mathrm{m \, s^{-1}}$) along a 1.25 m long tube as a function of distance z from the bottom of the hopper. Theoretical grain and air velocity profile: $v(z)$ (—) and $v_a(z)$ (- - -). ▲, Grain cluster velocity determined from spatio-temporal diagram at $z = 0.4$ m; ●, mean grain velocity computed from experimental particle fraction profile.

3.4. *Particle and air velocities in the stationary free-fall regime*

By combining the two mass conservation equations (3) and (4) and the particle fraction profile $c(z)$, one obtains the respective profiles $v_a(z)$ and $v(z)$ of the mean air and particle velocities. Theoretical curves obtained by taking into account the finite Reynolds number and density effects on the drag as well as grain friction with the walls are plotted in figure 4. One observes a decrease of the air velocity with distance (corresponding to the decreasing particle fraction) while, on the contrary, the grain velocity increases. In the upper part of the tube, the air moves faster than the grains and contributes to their acceleration. The velocities become equal around $z = 0.2$ m where pressure is minimal. Then the grains move faster than the air and their acceleration decreases until their weight is exactly balanced by friction with the air and with the walls.

These data are first compared to semi-experimental values determined by substituting into equations (3) and (4) experimental particle fractions plotted in figure 3(*a*). The good agreement between the two set of values essentially mirrors the agreement between theoretical and experimental particle fraction variations. More meaningful comparisons can be made with direct velocity determinations using the spatiotemporal diagram of figure 2. As already stated, the particle density fluctuations give rise to a set of parallel dark and light lines: the slope $\mathrm{d}z/\mathrm{d}t$ of these lines is equal to the propagation velocity of the fluctuations which is thus defined well at a given height. The velocity determined in this way at $z = 0.4$ m has been plotted on figure 4. It is close to the theoretical particle velocity although slightly lower. The difference is probably due to the fact that the linear camera does not have a sufficiently good spatial resolution to detect individual particles. Thus the fine dark and light lines of figure 2 probably correspond to small clusters of particles or to small low-density zones which may have a different velocity from that of individual grains: the fair agreement displayed in figure 4 indicates that these diagrams however represent a good practical way to track particle motions quantitatively.

Studying the stationary free-fall regime has allowed us to test measurement and modelling tools in a simple experimental case. It has been possible in particular to estimate quantitatively the magnitude of friction forces of the particles with the walls without making assumptions about the expression for the friction force between the air and the particles. Using a simple classical model for this latter force allowed us in addition to predict precisely pressure and particle fraction variations with distance. The estimate of particle cluster velocities from spatio-temporal diagrams has also demonstrated the potential of this technique for analysing the flow dynamics.

We shall now apply the same approach to the analysis of the density-wave regime characterized by a sequence of plugs and low-density bubbles moving downwards at a constant velocity v_w (Raafat *et al.* 1996). This system is more complex and new characteristic variables must be introduced such as the velocity v_w and the length of the bubbles and the plugs. Both the particle fraction and the air and grain velocities differ in the plug and bubble regions and the flow can be considered as stationary only in the reference frame moving at velocity v_w. In this part of the work, our objective is to analyse the dependence of the structure of the flow (particle fraction distribution, plug and bubble lengths, plug, particle and gas velocities, etc.) on the grain flow rate and to determine the relations between the pressure gradient, the wall friction forces and the various experimental variables.

4. Constant-velocity density-wave regime

4.1. *Spatio-temporal characteristics of the constant-velocity wave regime*

Spatio-temporal diagrams obtained in the wave regime at two different flow rates are displayed in figure 5(a, b). The sequence of plugs and bubbles appears as inclined stripes of slope corresponding to the plug velocity v_w. This slope is quite constant for a given plug and also from one plug to another so that v_w can be determined precisely. The variation of v_w with the flow rate q is seen in figure 6 to be roughly linear for large $q(q > 0.16 \, \mathrm{m \, s^{-1}})$ and constant for small q: plugs move faster near the transition to the free-fall regime where they disintegrate. Extrapolating the variation of figure 6 suggests that v_w would go to zero at a positive non-zero value of q (transient-wave regimes with stationary plugs were also observed in a tube closed at the bottom and filled from the top). A net downward grain flow from one plug to the next is observed. Inside each bubble, the spatio-temporal diagram is qualitatively similar to that in the free-fall regime: the curvature of the lines (figure 5a) indicates an acceleration of the grain clusters as they fall out of a plug. The distribution of the plugs is variable: in some cases plugs and bubbles are well-defined and separated while, in others, plugs cluster together (but remain separated) and buildup a like kind of 'puff pastry' as can be seen in figure 5(a).

The sequence of plugs and low-density bubbles does not extend down the full length of the tube: in the top part, it becomes established only after a distance of 4 to 15 cm below the hopper (increasing with flow rate q) where short plugs appear and quickly grow to their final length (figure 5a, b). Closer to the hopper, the spatio-temporal diagram is similar to that observed in the free-fall regime (figure 2) with a velocity increasing with distance. At the other end, the lower part of the tube (not visible on the figure) is occupied by a compact bottom plug of length l_{bp} decreasing from more than 300 mm down to 50 mm as q increases (figure 9).

Information provided by the spatio-temporal diagrams is complemented by particle fraction measurements. Figure 7 displays the time variation of the capacitance sensor
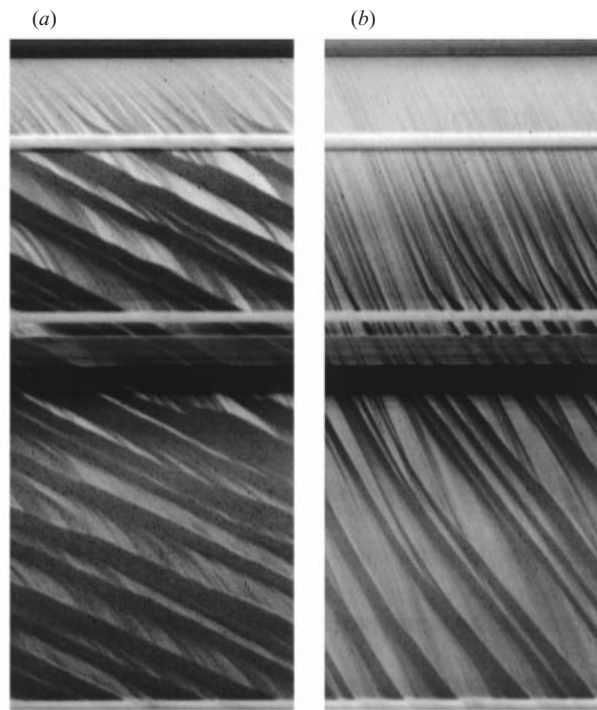
FIGURE 5. Spatio-temporal images of the fluctuations of particle distribution along the tube obtained with a linear camera in the wave regime. Line sampling rate: 2000 Hz, height of field of view: 450 mm, time lapse corresponding to diagrams: 0.5 s. (*a*) $q = 0.14 \, \text{m s}^{-1}$, (*b*) $q = 0.22 \, \text{m s}^{-1}$. The spatio-temporal diagrams extend from the top of the tube (the bottom of the hopper appears as a dark strip at the top). Both horizontal white lines correspond to mechanical supports and the dark stripe below to a pressure transducer.
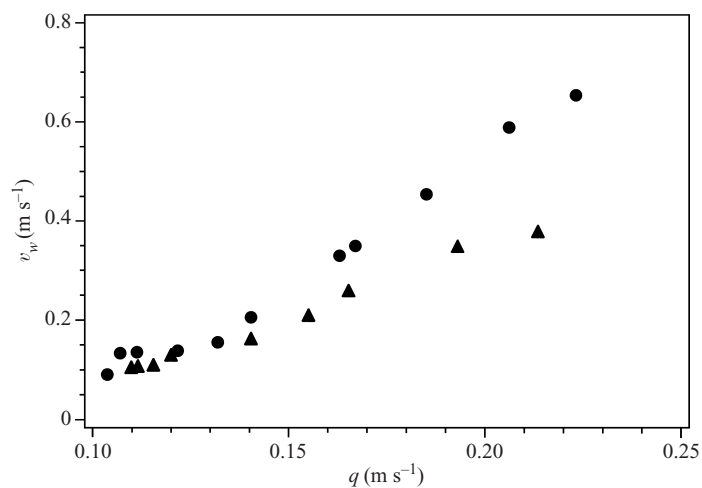

FIGURE 6. Wave velocity v_w as a function of the superficial grain velocity q in the steady waves regime (v_w is computed from the spatio-temporal diagram). ●, Data points corresponding to beads with a smooth surface; ▲, data points for beads with a rougher surface.
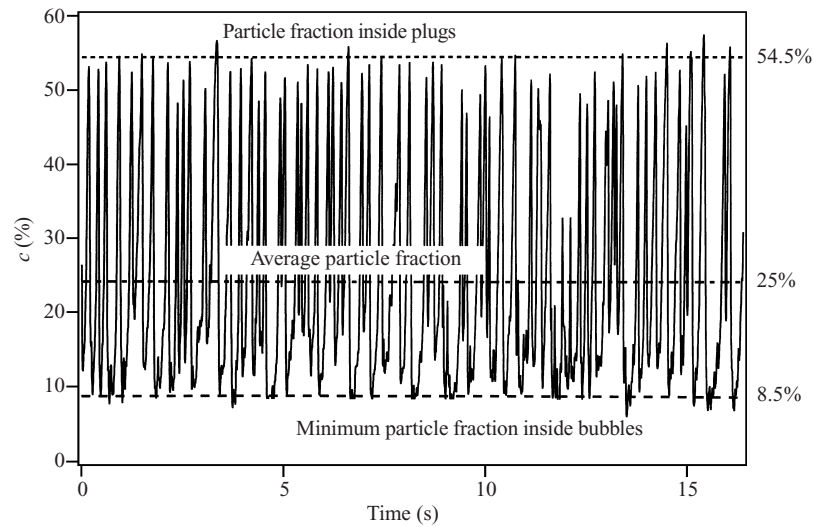
FIGURE 7. Time variation of the reading of a capacitive particle fraction sensor located at 300 mm below the hopper in the density-wave regime ($q = 0.1 \, \text{m s}^{-1}$), particle fraction inside plugs $= 54.5\%$, average particle fraction $= 24\%$, minimum particle fraction inside bubbles $= 8.5\%$.

in the wave regime, showing large fluctuations of the particle fraction between well-defined high values of often 50% or more in the plugs and low values of 15% or less inside bubbles. The asymmetrical peaks correspond to the plugs: the sharper rear slope of the peak corresponds to the upper side of the plugs where the particle fraction increases abruptly as grains falling through a bubble hit the top of the plug. On the other hand, the particle fraction variation is smoother at the bottom of the plugs where beads accelerate progressively as they leave it. The particle fraction c_p in the plugs is more or less constant from one plug to the next while the minimum particle fraction c_b inside bubbles increases with their length. This reflects the acceleration of particles inside bubbles and the fact that they reach a higher velocity at the bottom of long bubbles. The distribution of the size of the plugs and the bubbles can be estimated from the width of the peaks and their intervals together with direct measurements of the plug velocities: in a previous work (Raafat *et al.* 1996), the size of the plugs was found to be relatively constant and of the order of 10 mm while bubbles are generally larger and with more dispersed sizes (no indication of very broad size distributions, such as power laws for instance, was found however). Variations of the mean bubble sizes with the flow parameters are displayed below in figure 9.

Figure 8 presents, for beads with a smooth surface, variations with the superficial velocity q of four specific particle fractions: the fraction c_p in the plugs, the minimum fraction c_b at the bottom of long bubbles, the time-averaged fraction $\bar{c}$ and the fraction c_{bp} in the bottom plug near the outlet of the tube. The particle fraction c_p in the plugs decreases from 60% for $q = 0.11 \, \text{m s}^{-1}$ (close to the particle fraction of a fixed random packing) down to 30% for $q = 0.23 \, \text{m s}^{-1}$ with an acceleration of the variation close to $q = 0.16 \, \text{m s}^{-1}$ (the same value above which the wave velocity v_w increases faster with q). The minimum fraction c_b in the bubbles is of the same order of magnitude as in the free-fall regime; the time-averaged fraction $\bar{c}$ is of the order of 25% at low flow rates and decreases quickly with q towards an almost constant value of 20%. The particle fraction c_{bp} in the bottom plug is larger than that of the
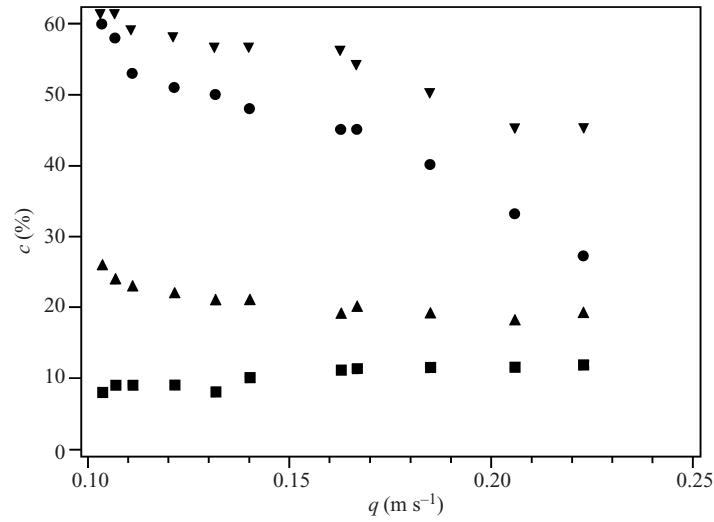
FIGURE 8. Variations of time-averaged particle fraction $\bar{c}$ (▲), particle fraction in plugs c_p (●), particle fraction inside bubbles c_b (■), and bottom plug particle fraction c_{bp} (▼) in the wave regime as a function of superficial grain velocity q.
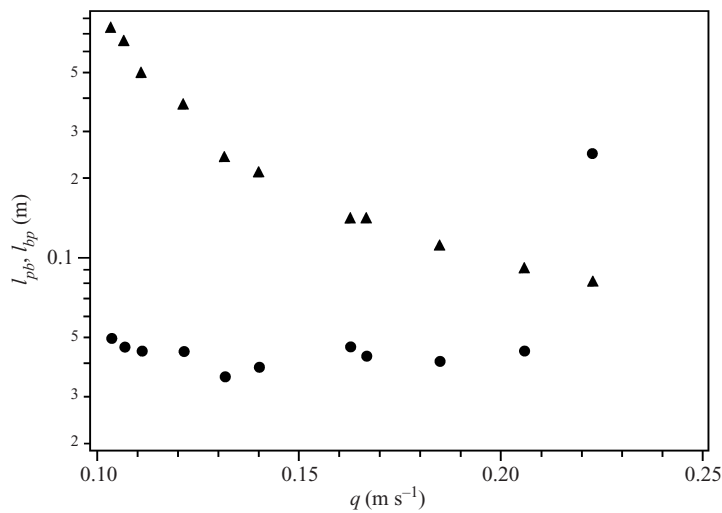

FIGURE 9. Variation of the mean plug+bubble length $l_{pb} = l_p + l_b$ (●) and of the bottom plug length l_{bp} (▲) as a function of the superficial grain velocity q.

moving plugs and is approximately constant and of the order of 55% for q below $0.16\,\mathrm{m\,s^{-1}}$ (5–7% less than a fixed packing); it then decreases towards 45%.

Spatio-temporal diagrams and particle fraction variations with time also allow us to determine the mean length l_{pb} of the elementary cells including a plug and a bubble. It is taken equal to the mean time interval between two particle fraction peaks divided by the wave velocity v_w: its variations and those of the length of the bottom plug l_{bp} are plotted in figure 9 as a function of q. The mean value of the cell length l_{pb} is almost constant with q and of order 40 mm up to the transition to the free-fall regime. On the other hand, the length of the bottom plug steadily decreases: at the transition between the wave and free-fall regimes, l_{bp} is less than 50 mm.
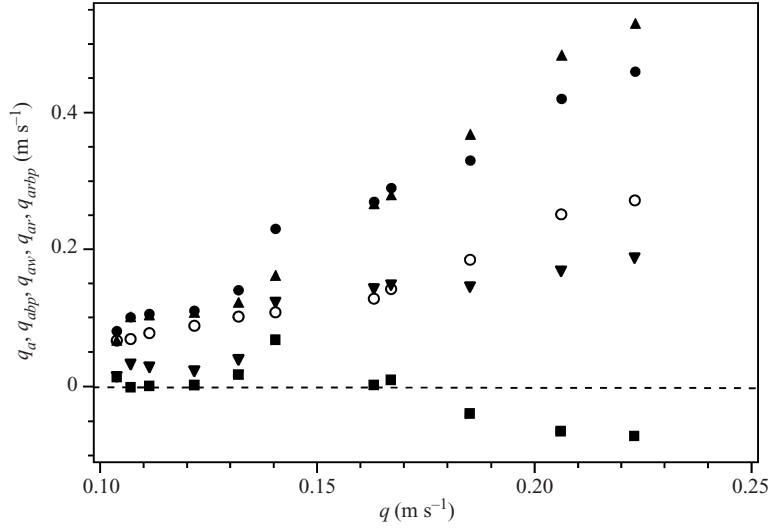
FIGURE 10. ●, Mean superficial velocity q_a of air. ○, Superficial air velocity component q_{abp} corresponding to passive entrainment in the bottom plug. ▼, Superficial air velocity component q_{arbp} corresponding to the relative motion of air with respect to the grains in the bottom plug. ▲, Superficial air velocity component q_{aw} corresponding to wave motion. ■, Superficial air velocity q_{ar} measured in a reference frame moving at velocity v_w. All velocities are plotted as a function of the superficial grain velocity q.

At this stage, the structure of the density-wave flows and the corresponding particle distributions have been determined as a function of the grain flow rate: in all cases, one observes a constant-velocity motion of dense plugs with a particle fraction sometimes barely lower than that of a static packing and decreasing at large grain flow rates. We shall now investigate the kinematical properties of the system by evaluating the flow components of the air and of the grains, both associated with the global motion of the wave system and relative to this moving reference frame.

4.2. *Global and relative flow components*

The mean superficial air velocity q_a in the tube section is computed by means of equation (2) from the reading Q_{meas} of the air flow sensor at the inlet of the hopper. Figure 10 displays the variations of q_a (filled circles) as a function of q: the velocity q_a increases at first linearly with q but is always 3–10 times smaller than in the free-fall regime. Both q and q_a result from the combination of a global mean motion at the wave velocity v_w and a relative motion of both the air and the grains with respect to the plug boundaries. An interesting feature of the reference frame moving at the velocity v_w is that plugs and bubbles appear fixed: the flow distribution is therefore stationary which makes writing conservation equations easier. We also assume that the plug and bubble lengths l_p and l_b are constant with time and from one cell to another.

Let us estimate now the relative magnitude of the different flow components: we denote as u_a and u the respective air and grain velocities in the moving reference frame and as v_a and v the corresponding values in the laboratory frame. Then

$$v = u + v_w, \quad v_a = u_a + v_w. \tag{12a,b}$$

The relative velocities u_a and u are constant with time at a fixed point in the moving frame. In the same way, let us denote as q_{ar} and q_r the superficial velocities of the air

and the grains in the moving frame: they are constant with both time and distance (due to mass conservation) and satisfy

$$q_{ar} = u_a(1-c), \quad q_r = uc, \tag{13a,b}$$

in which c is the local particle fraction. The differences between q_{ar} and q_r and the corresponding superficial velocities q_a and q in the laboratory frame are the volume-averaged superficial velocities $q_w = v_w\bar{c}$ and $q_{aw} = v_w(1-\bar{c})$ which represent the flow rates associated with the global wave motion. The relative superficial velocities in the moving frame thus satisfy

$$q_{ar} = u_a(1-c) = q_a - v_w(1-\bar{c}), \quad q_r = uc = q - v_w\bar{c} \tag{14a,b}$$

Variations of these superficial velocities q_{ar}, q_{aw}, q_r, q_w as function of the global grain superficial velocity q are plotted in figures 10 (for the air) and 11(a) (for the grains). In agreement with previous results (Raafat *et al.* 1996) the relative superficial velocity of the grains q_r varies little with the flow rate (particularly for $q > 0.12\,\mathrm{m\,s^{-1}}$) and does not vanish when the wave velocity goes to zero.

Grain and air velocities in the different parts of the flow can now be determined by using equations (12a,b) and (13a,b) and the particle fractions from figure 8. Figure 11(b) displays variations of u and u_a determined in this way both in the plugs (u_p and u_{ap}) and at the end of the bubbles (u_b and u_{ab}). Since velocity is continuous at the lower plug–bubble boundaries, u_p is also the grain relative velocity at the top of the bubbles. Figure 11(b) shows therefore that this relative velocity u increases by a factor of 3 to 10 between the top and the bottom of the bubbles (in agreement with the curvatures of the streaks in the spatio-temporal diagram); u is however smaller than in the free-fall regime since the acceleration distance is shorter (the terminal velocity is not reached) and the downflow of air accelerating the beads is negligible. The relative air velocity q_{ar} is either very small or negative: this implies that the upward permeation of the air through the plugs induced by the mean pressure gradient balances the passive drag by the downwards motion of the grains.

An interesting issue is the value in the moving reference frame of the initial relative velocity u_p of grains leaving a plug. We suggest that the bottom layers of the plug detach sequentially one after another due to the dilatancy which is required to deform the plug. Let us call τ the time interval between the detachment of two successive grain layers, each of typical thickness $2a$. Then $u_p = 2a/\tau$. Let us assume that, after the detachment, the motion of the layer corresponds to a free fall, neglecting air friction. Then, the spacing h_R between two layers at the time when the second layer becomes detached should be $h_R = \frac{1}{2}g\tau^2$. One expects the value of h_R to be a few microns – a small percentage of the grain diameter. The values of h_R computed in this way from the experimental values of u_p displayed in figure 11(b) range between 4 and 15 µm, in agreement with these expectations (the variation is explained by the variable particle fraction of the plugs which will modify the locking between grains).

A similar decomposition of the global air flow rate q_a can be performed in the bottom plug (taking this time the flowing grains as the moving reference frame). A first component of q_a is the volume q_{abp} of air per unit time and unit area dragged by the flowing grains:

$$q_{abp} = \frac{q}{c_{bp}}(1 - c_{bp}). \tag{15}$$

This value q_{abp} and the difference $q_{arbp} = q_a - q_{abp}$ are also plotted in figure 10 (open circle and downward triangle symbols). The difference q_{arbp} would be equal to q_a if
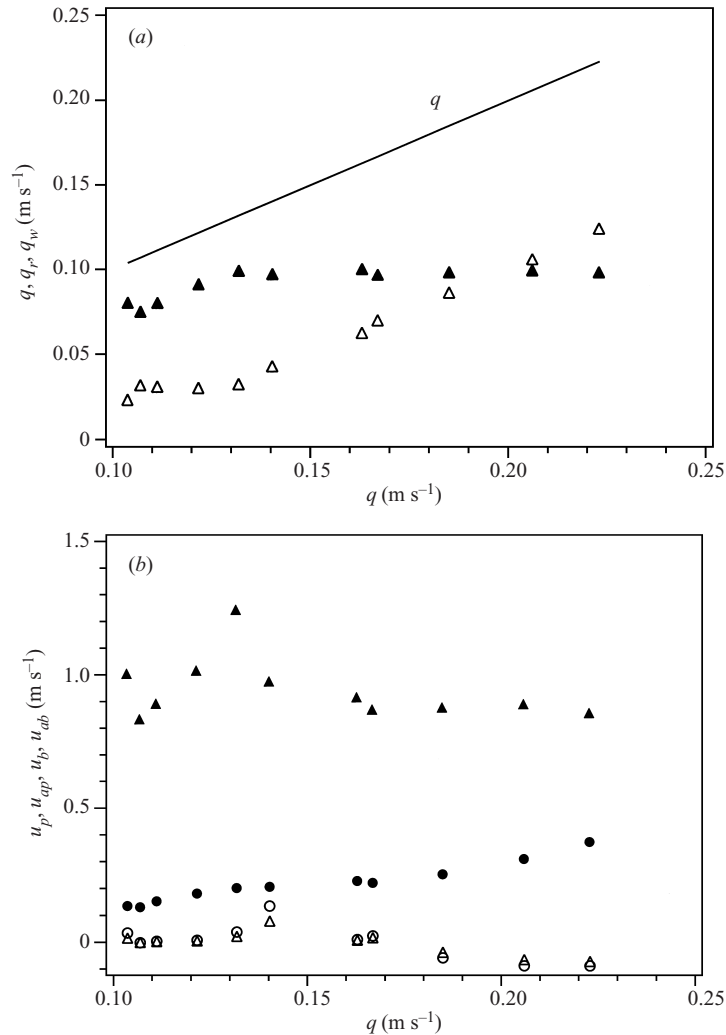
FIGURE 11. (*a*) Variation of grain superficial velocity q_r(▲) measured in the moving frame and of component q_w(△) corresponding to the global wave motion, as a function of the total superficial velocity q (also displayed as a continuous line as a reference). (*b*) Variation of local grain velocity relative to reference frame of velocity v_w for air (index a) and grains in plugs (u_{ap}(○) and u_p(●)) and at the bottom of bubbles (u_{ab}(△)) and u_b(▲)) as a function of grain superficial velocity q.

the air had no relative motion with respect to the grains in the bottom plug. This is indeed the case at low flow rates ($q < 0.14\,\text{m}\,\text{s}^{-1}$) for which the bottom plug is long ($l_{bp} > 200\,\text{mm}$ from figure 9) and compact ($c_{bp} > 55\%$ from figure 8). At higher flow rates both the particle fraction and l_{bp} decrease so that the relative motion of the air and the grains is no longer negligible: as can be seen in figure 10, the global flow rate q_a is then markedly higher than q_{abp} due to the downwards air flow induced by the pressure gradient through the bottom plug (these permeation components are estimated below).

The previous discussion has demonstrated that the density-wave flows can be separated into a component representing passive transport of the air and the grains at the wave velocity v_w and components corresponding to their relative motion with
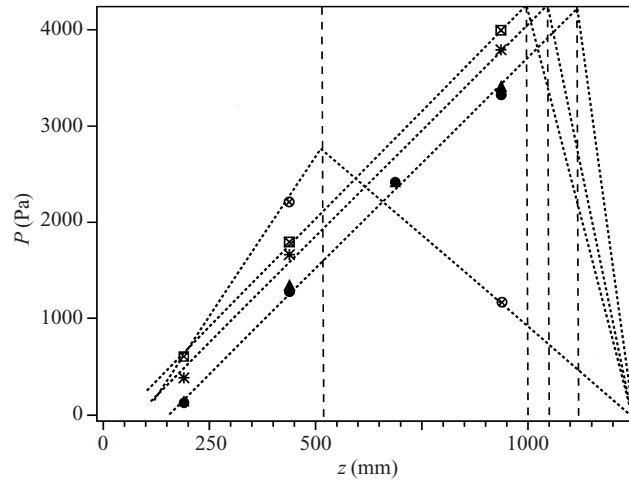
FIGURE 12. Pressure variations as a function of distance along the tube for different superficial grain velocities: ▲, $q = 0.2\,\mathrm{m\,s^{-1}}$; ●, $q = 0.19\,\mathrm{m\,s^{-1}}$; ✳, $q = 0.16\,\mathrm{m\,s^{-1}}$; ⊗, $q = 0.35\,\mathrm{m\,s^{-1}}$; ⊠, $q = 0.135\,\mathrm{m\,s^{-1}}$. Dotted lines correspond to linear regressions over the data and to assumed variations in the bottom part of the tube.

respect to the plugs–bubbles sequence. The relative air and grain flow rates in this moving frame are almost constant with q as well as the mean length of the plug–bubble pairs: this leads to the approximate picture of a flow with roughly constant characteristics in the moving frame but dragged along at the velocity v_w varying with q. In order to obtain a more precise picture the pressure gradient distribution will now be investigated: it plays a key role both in determining the permeation of the air through the dense parts and in the balance of the weight of the grains so that they reach a constant velocity.

4.3. *Pressure profiles and pressure gradient in the density-wave regime*

Time-averaged pressures obtained from the four sensors are displayed in figure 12 as a function of distance from the hopper, for different grain superficial velocities q. In contrast with the case of the free-fall regime (figure 3*b*), the pressure inside the tube is generally higher than the atmospheric pressure p_{at}; even at the very top of the tube, it is of the order of p_{at}. The pressure increases approximately linearly with distance down the part of the pipe occupied by the sequence of plugs and bubbles. Inside the bottom plug, the flow is steady: the particle fraction and air and grain velocities can then be assumed to be constant with both distance and time so that the pressure gradient is also constant with distance. Pressure decreases linearly, therefore, along the bottom plug down to atmospheric pressure at the outlet (see dashed lines). A data point fully compatible with this hypothesis is obtained for $q = 0.35\,\mathrm{m\,s^{-1}}$ on the pressure port located at $z = 950\,\mathrm{mm}$ (figure 12) which at this flow rate is located inside the bottom plug (for other flow rates, all pressure ports are inside the wave region).

Finally, one observes that the pressure drop across the packed grains in the hopper is small compared to that across the bottom plug (the pressure at the top of the tube is close to atmospheric pressure). This is due to the fact that, in the hopper, pressure gradients are localized over a distance of a few mm from the outlet due to its conical shape while the bottom plug is several cm long and of constant, small, diameter. The pressure profile measurements demonstrate therefore the important contribution of
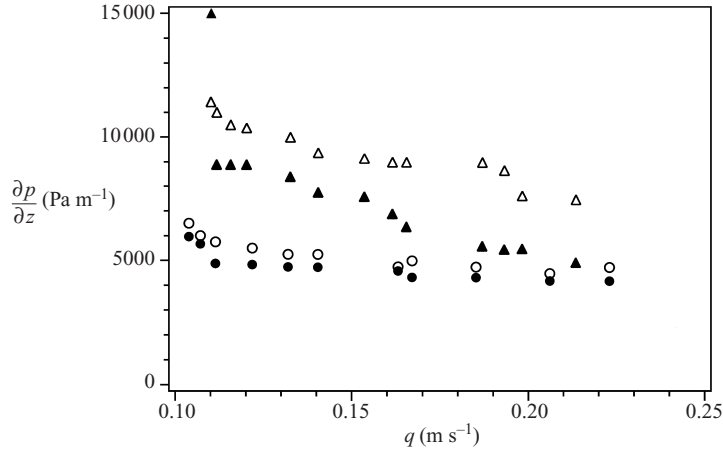
FIGURE 13. Variations of pressure gradients in the wave regime as a function of the superficial grain velocity q. Pressure gradients measured experimentally: ▲, for rough grains; ●, for smooth grains. Pressure gradients corresponding to the weight of the grains: ○, for smooth and △, rougher grains.

the bottom plug to the stability of the density-wave regime: it allows the build-up of a strong pressure gradient along the plug–bubble sequence while avoiding inducing a large downward air flow which might destroy the plugs (as happens near the transition between the wave and free-fall regimes).

Figure 13 (filled circles) displays variations with the velocity q of the experimental pressure gradient $\partial p/\partial z$ (equal to the slope of the linear part of the curves of figure 12): $\partial p/\partial z$ decreases by about 30% as q increases from 0.1 to 0.23 m s^{-1}.

In the two next sections, we analyse how these pressure data and momentum conservation equations can be used to determine first the wall friction in the wave regime and then permeation flows due to the non-zero permeability of the dense regions (moving plugs and bottom plug) which play a very important part at high flow rates in the transition towards the free-fall regime.

4.4. *Momentum conservation and wall friction in the density-wave regime*

In order to determine the wall friction force, we shall use a similar approach as in the free-fall regime and write the equivalent of equation (8) as

$$\overline{\frac{\partial p}{\partial z}} = \rho_g g \bar{c} - \frac{(F_w)_{bp}}{(l_p + l_b)\pi R^2} \tag{16a}$$

Here, $\overline{\partial p/\partial z}$ is the pressure gradient averaged over the bubble–plug cell. Equation (16a) is written in the reference frame moving at the wave velocity v_w so that the flow can be considered as stationary: it reflects the balance among the pressure gradient, the mass of the grains and the friction force $(F_w)_{bp}$ over the length of a bubble + plug cell. This equation has been written over a cell length in order to be able to consider than the momentum of the particle entering the cell is equal to that of particles leaving it. An equivalent relation can be written over a sequence of consecutive cells leading to the more general equation

$$\overline{\frac{\partial p}{\partial z}} = \rho_g g \bar{c} - \frac{\bar{F}_w}{\pi R^2}. \tag{16b}$$

Here, $\bar{F}_w$ is the mean friction force per unit length – taken positive when oriented towards the bottom. Equation (16*b*) will remain approximately valid even if the sequence is not exactly periodical provided the momentum difference between particles leaving and entering at the end of the sequence is not too large. As in the free-fall regime, and since the air flow velocity is much lower than in this latter case, we shall consider that the friction force of the air with the walls is negligible and that $\bar{F}_w$ is mostly due to the friction force of grains with the walls.

In order to estimate $\bar{F}_w$ we have plotted on figure 13 (open circles for smooth new beads) variations of $\rho_g g\bar{c}$ computed from the data of figure 8. At a given q, the weight $\rho_g g\bar{c}$ is barely lower than $\partial p/\partial z$ so that, taking into account the experimental errors, F_w should not be higher than 10% of the grain weight, i.e. certainly lower than in the free-fall regime. We conclude that, for the corresponding set of smooth beads, the momentum balance largely results from an almost 'hydrostatic' equilibrium between the weight of the grains and the pressure gradient. Since most of the mass of the grains is localized in the plugs, we expect the pressure gradient also to be higher inside the plugs than inside the bubbles. This low wall friction and the weak dependence of the pressure gradient on the grain flow rate confirm the previous intuitive picture already suggested at the end of §4.2, namely that the flow in the moving reference frame depends very little on the global grain flow rate q, which affects only the global drift of the plug–bubble sequence.

4.5. *Permeation of air through the moving plugs*

The permeation of air through the plugs is a key factor limiting the stability of the density-wave regime: it is driven by the pressure drop across the plugs (which is large enough to balance most of their weight) and limited by their permeability. If the particle fraction in the plugs decreases with q (as in figure 8) their permeability increases: the flow rate necessary to build up a pressure gradient balancing the weight of the grains becomes too large and the transition towards the free-fall regime occurs. The relative air–grain velocity of the permeation flow is related to the pressure drop Δp_p over the length of a plug by Darcy's law:

$$(u_{ap} - u_p)(1 - c_p) = -\frac{K(c_p)}{\eta}\frac{\Delta p_p}{l_p} \tag{17}$$

in which $K(c_p)$ is the permeability of the plug, η is the viscosity of air and the factor $(1 - c_p)$ is used to determine the superficial flow rate per unit area. As a first approximation, one can estimate that Δp_p, is of the order of the pressure drop $l_{pb}\overline{\partial p/\partial z}$ over the full cell (the friction forces should be concentrated in the plugs and most of the grain mass which controls the term $\rho_g g c(z)$ is also localized there). Table 1 lists Δp_p values obtained in this way using data from figures 9 and 13. Estimating l_p from the spatio-temporal diagrams then allows determination of an experimental plug permeability value $K(c_p)$ by applying (17) and using values of c_p, u_p and u_{ap} displayed above in figures 8 and 11(*b*). The corresponding values of $K(c_p)$ and l_p are also in table 1 together with a theoretical estimate K_{CK} of the plug permeability obtained from the classical Carman–Kozeny relation:

$$K_{CK} = \frac{(1 - c)^3 d^2}{180\,c^2}, \tag{18}$$

valid for packings of monodisperse spheres of particle fraction c and diameter d (d is equal to 175 μm and c is taken to be c_p). The two values are in fair agreement, taking into account the uncertainty in the values of the plug length l_p and of the pressure

q (m s^{-1})	Δp_p (Pa)	l_p (m)	K (Darcy)	K_{CK} (Darcy)
0.104	295	0.01	25	30
0.107	260	0.01	39.5	37.5
0.111	215	0.01	60	63
0.121	213	0.01	33.5	77
0.132	168	0.01	90	85
0.140	181	0.01	38	104
0.163	208	0.008	85	140

TABLE 1. Variations with the grain superficial velocity in the density-waves regime of the pressure drop on the plugs, the plug length l_p and the plug permeability as estimated from the experimental results (K) and from Carman–Kozeny's formula using the measured plug porosity (K_{CK}).

drop Δp_p over the plug. No values are listed for larger flow rates ($q > 0.16$ m s^{-1}): the uncertainties are indeed too large due to the increase of the pressure gradient in the bubbles compared to that in the plug and to the decrease of l_p which becomes very difficult to determine precisely. An important feature of the results of table 1 is the strong increase (by a factor of 4) of the permeability with the grain flow rate q (this increase should be even greater at higher flow rates): this confirms that the increase of the permeation of air through the plugs at high flow rates will result in a transition towards the free-fall regime.

4.6. *Permeation of air through the bottom plug*

The bottom plug observed in the present experiments also plays an important role. First, it must withstand a pressure difference equal and opposite to that built up along the plug–bubble sequence. The corresponding force is, in this case, oriented in the same direction as the weight of the grains. The downwards resultant force must then be balanced by friction forces on the walls and on the constriction at the bottom of the tube (the complex geometry of the latter makes a direct evaluation difficult). But the influence of the constriction should be felt only over a vertical distance of the order of the Janssen length. Second, the finite permeability of the bottom plug reduces the downflow of air induced by this pressure difference: if this permeability is too large and/or the bottom plug is too short, the velocity of air (and the wave propagation velocity) increases and the plugs–bubbles system finally disintegrates. The relative flow rate q_{arbp} of air through the moving grains due to the finite permeability of the bottom plug is equal to $q_a - q_{abp}$. The experimental value q_{arbp} computed in this way is plotted in figure 10 and listed in table 2 as a function of the grain superficial velocity q. As for the moving plugs, a theoretical value q_{arbp}^{th} of this relative flow rate can be obtained by estimating the permeability $K(c_{bp})$ of the bottom plug through the Carman–Kozeny relation (18) using the measured value c_{bp} of the particle fraction; q_{arbp}^{th} is then obtained by applying Darcy's law to the bottom plug:

$$q_{arbp}^{th} = \frac{K(c_{bp})}{\eta} \left| \frac{\partial p}{\partial z} \right| \frac{L - l_{bp}}{l_{bp}}. \tag{19}$$

Here the pressure difference has been taken equal and opposite to the global pressure difference along the total length ($L - l_{bp}$) of the wave section and $\partial p / \partial z$ is the pressure gradient in this region. Both the values of q_{arbp}^{th} and those of the permeability $K(c_{bp})$ are listed in table 2. Both sets of values are of the same order of magnitude up to $q = 0.18$ m s^{-1}: deviations seem due to experimental uncertainties. The larger

q (m s^{-1})	q_{arbp} (m s^{-1})	K_{bp} (Darcy)	q^{th}_{arbp} (m s^{-1})
0.104	0.015	27	0.006
0.107	0.032	27	0.007
0.111	0.027	33.5	0.013
0.122	0.022	37.5	0.022
0.132	0.038	44	0.047
0.140	0.122	44	0.055
0.163	0.142	46	0.091
0.167	0.148	57	0.105
0.185	0.145	85	0.206
0.206	0.168	140	0.409
0.223	0.188	140	0.464

TABLE 2. Variations with the grain superficial velocity of relative air superficial velocity with respect to the moving grains in the bottom plug; q_{arbp} = relative velocity determined from experimental flow measurements, K_{bp} = permeability of bottom plug computed from experimental particle fraction measurements by means of the Carman–Kozeny relation, q^{th}_{arbp} = relative air velocity estimated from the computed permeability of the bottom plug.

difference at higher flow rates may be due to spatial variations of the particle fraction in the bottom plug near the transition between the wave and the free-fall regimes.

As observed above, the relative air flow in the bottom plug q_{arbp} is almost negligible below $q < 0.14$ m s^{-1} and increases at high flow rates due to the lower values of both the bottom plug length and particle fraction. This increase of q_{arbp} coincides with a change in the behaviour of the other parameters, in particular a rapid increase of the wave velocity v_w and also a greater variation of the particle fraction in plugs. At higher flow rates, the relative air velocity and the wave velocity increase more rapidly, leading finally to a disintegration of the plug–bubble structure and to a transition towards the free-fall regime.

This set of results provides a global picture of the mechanical equilibrium in the wave regime for the type of grains we have used. The weight of the compact plugs is mostly balanced by the air pressure gradient (almost as in an 'hydrostatic' equilibrium) provided the permeability of the plugs is low enough to slow down their downwards motion and also that the permeability of the bottom plug is low enough to reduce the relative air flow through it. The friction of air and grains with the walls does not seem to play a major role for the smooth beads which we have used. In the next section, we investigate further these effects by performing the same experiments with beads with a rougher surface, which should enhance wall friction.

5. Density-wave regime dependence on the surface characteristics of beads

All experimental results presented up to now have been obtained with beads used only for a small number of experiments and which display a smooth and clean surface when observed with a microscope. After many experiments have been performed with a given set of beads, namely after they have passed a hundred times or so through the tube, their surface becomes rougher and microscopical impurities attach to the surface. Figure 14 displays particle fraction variations with the grain flow rate observed with such a set of rougher grains. Comparing these variations with those displayed in figure 8 for smooth beads, one observes that the particle fraction is always higher, particularly at higher superficial grain velocities for which the mean particle fraction
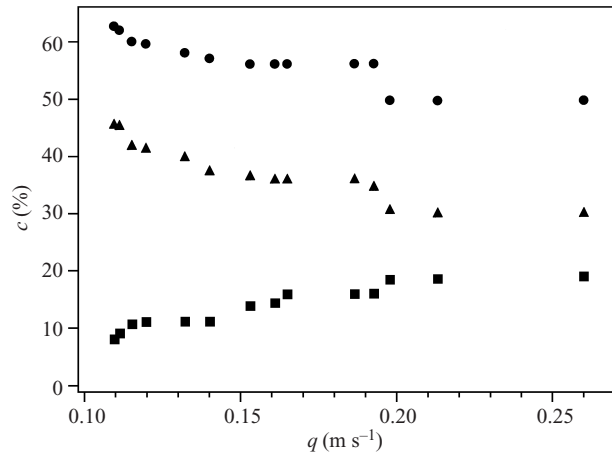
FIGURE 14. Variations of the time-averaged particle fraction $\bar{c}(\blacktriangle)$, of particle fraction in plugs $c_p(\bullet)$ and of minimum particle fraction $c_b(\blacksquare)$ inside bubbles for rough grains in the wave regime as a function of the superficial grain velocity q.

decreases much slower than in the previous case. The particle fraction in plugs is also higher and is very close at low flow rates to the typical values ($c = 63\%$) for static bead packings. It can also be seen in figure 6 that the wave velocity v_w is lower than for smooth beads above $q = 0.14\,\mathrm{m\,s^{-1}}$ and increases more linearly with q: the change of regime above 0.15 observed for the smoother beads does not appear. These results are confirmed by pressure gradient measurements displayed in figure 13. The difference between the measured pressure gradient and the term reflecting the weight of the beads is much higher than for smooth beads and represents up to 30–40% of the total gradient: this implies that the friction force F_w with the walls is increased in the same proportion.

We conclude that increasing the roughness of the bead surface enhances, as expected, the interaction between the grains and the walls; it also slows down significantly the wave motion and increases the particle fraction in the plugs and in the mean.

6. Oscillating-wave regime

6.1. *Experimental observations*

At low grain superficial velocities near the transition towards the compact regime (typically 0.085 to 0.11 m s^{-1}), the velocity of the plugs and of the bubbles is not always constant but in some cases oscillates around a non-zero drift velocity. Such effects are particularly observed for grains with a rough surface used for a long time in experiments. Figure 15(a) displays pressure variations with time measured at a distance of 450 mm for $q = 0.087\,\mathrm{m\,s^{-1}}$. The global amplitude of the oscillations is of the order of 10 000 Pa, which is very large and even higher than the mean value. The frequency spectrum of the pressure is displayed in figure 15(b): the first peak represents the oscillation frequency of order 5.7 Hz which is almost independent of the grain flow rate.

Physically, these oscillations may be modelled as vibrations of a sequence of masses (representing the plugs) connected by elastic springs (representing the bubbles): their low frequency results from the large density of the compact plugs and the high
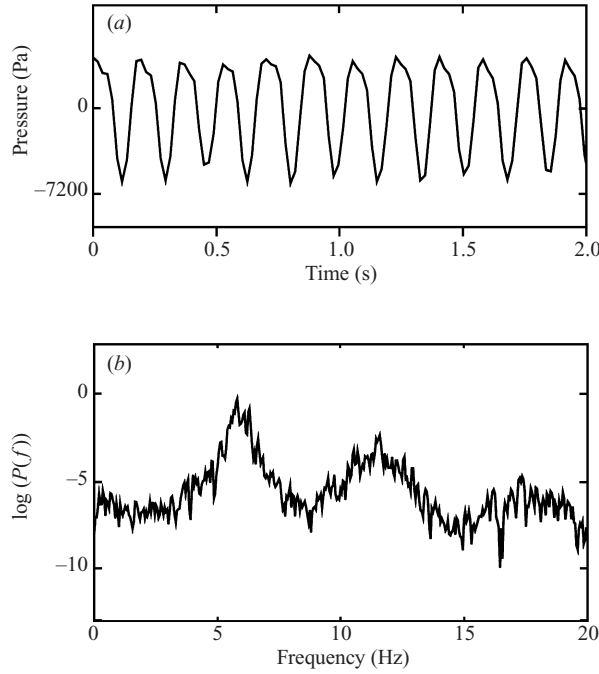
FIGURE 15. (*a*) Time variations of pressure in an oscillating density-wave flow ($q = 0.087\,\mathrm{m\,s^{-1}}$) at a distance of 450 mm below the hopper. (*b*) Logarithm of power spectrum of pressure variations in the same experiment.

compressibility of the low-particle-fraction bubbles. An alternative point of view is to consider the system as a two-phase flow (similar to air–water for instance) in which both the mean density and the compressibility are high: they are characterized by a very small sound velocity of the order of a few $\mathrm{m\,s^{-1}}$ resulting in low resonance frequencies. There are two main damping mechanisms: wall friction, mostly in the region of the plugs, and viscous dissipation, due to the flow of air through the plugs.

6.2. *Simplified set of equations describing the oscillating-wave regime*

We model these oscillations by adding to the previous equations time-dependent terms corresponding to variations of the length l_b of the bubbles, the plug velocity v_p and pressure (the plug length and particle fraction are taken constant). These variables vary from one plug + bubble cell (denoted by an index j) to the next and are assumed to oscillate about a mean value corresponding to the constant-velocity regime discussed above (for instance the wave propagation velocity is still v_w). Each parameter is then the sum of a constant part (no index) and of a periodic oscillatory component (index 1), assumed to be small enough to neglect second-order terms. All conservation equations are written in the reference frame moving at velocity v_w. The volume conservation of grains and of air between sections of two successive plugs is then

$$(c_b(l_b) - c_p)\frac{\mathrm{d}l_{bj}^1}{\mathrm{d}t} = q_j^1 - q_{j+1}^1. \tag{20}$$

and

$$(c_p - c_b(l_b))\frac{\mathrm{d}l_{bj}^1}{\mathrm{d}t} = q_{aj}^1 - q_{aj+1}^1 - \chi l_b(1 - \overline{c_b})\frac{\mathrm{d}p_j^1}{\mathrm{d}t} \tag{21}$$

(the superficial velocities q and q_a are defined inside the plugs). The second equation includes a term equal and opposite to the variation of the volume of grains and a term due to the compressibility: $\chi = -1/v \partial v/\partial p$ of air. The particle fraction $c_b(l_b)$ is the particle fraction at the bottom of the bubbles (the minimum value) and $\overline{c_b}$ is the average particle fraction in the bubbles.

The non-stationary part of the equation of motion of the plugs can be written as

$$\rho_g l_p \frac{\mathrm{d}q_j^1}{\mathrm{d}t} = p_{j-1}^1 - p_j^1 - \frac{F_{wj}^1}{\pi R^2}, \tag{22}$$

where F_{wj}^1 is the varying part of the friction force (assumed localized on the plug) in cell j. A final equation relates, through Darcy's law, time-varying pressure differences across a plug to the relative velocity of air and grains inside it:

$$q_{aj}^1 - \frac{1 - c_p}{c_p} q_j^1 = \frac{K(c_p)}{\eta} \frac{p_{j-1}^1 - p_j^1}{l_p}. \tag{23}$$

Let us consider a progressive sine-wave perturbation of angular frequency ω and wave vector k: the length of bubble j (the index starts at 1 for the topmost plug and the bubble just below) and the pressure inside it satisfy

$$l_{bj}^1(t) = l_b^1 \exp[\mathrm{i}(\omega t - jk(l_p + l_b))], \tag{24}$$

$$p_j^1(t) = p^1 \exp[\mathrm{i}(\omega t - jk(l_p + l_b))]. \tag{25}$$

The time-varying components $q_j^1(t)$ and $q_{aj}^1(t)$ of the air and gas flow rates have similar expressions with complex amplitudes q^1 and q_a^1. Substituting these expressions into (20–24) and neglecting the friction term F_w^1 yields a system of linear equations which has a solution if

$$-\omega^2 + \frac{4\mathrm{i}\omega K(c_p) \sin^2(\frac{1}{2}k(l_p + l_b))}{\eta \chi l_p l_b (1 - \overline{c_b})} + \frac{4 \sin^2(\frac{1}{2}k(l_p + l_b))}{\rho_g \chi l_p l_b c_p (1 - \overline{c_b})} = 0. \tag{26}$$

This dispersion equation includes the damping effect of viscous dissipation of gas flowing through the plugs (middle term). If this term is neglected, (26) closely resembles classical dispersion relations for mass–spring chains. In the limit of long wavelengths (low wave vectors such that $k(l_p + l_b) \ll 1$), ω/k tends towards a constant limit representing the propagation velocity c_{osc} of low-frequency oscillations of the plugs:

$$c_{osc} = \frac{\omega}{k} = \frac{l_p + l_b}{\sqrt{\rho_g \chi l_p l_b c_p (1 - \overline{c_b})}}. \tag{27}$$

This velocity is of the order of the sound velocity $1/\sqrt{\chi \rho_g}$ corresponding to an hypothetical fluid with the compressibility χ of the air and the density ρ_g of glass. Other factors are geometrical terms taking into account the relative volumes occupied by air and grains.

6.3. Experimental orders of magnitude of the wave oscillation parameters

Using experimental values from previous sections ($l_b = 0.02\,\mathrm{m}$, $l_p = 0.01\,\mathrm{m}$), equation (27) provides the estimate $c_{osc} = 23\,\mathrm{m\,s^{-1}}$. The experimental oscillation frequency $f_{osc} = 5.7\,\mathrm{Hz}$ corresponds therefore to a wavelength $\lambda_{osc} = c_{osc}/f_{osc} = 4.1\,\mathrm{m}$. The oscillations observed can be considered as stationary resonant modes excited by velocity fluctuations at the outlet of the hopper: the hopper outlet (which communicates with the outside atmospheric pressure through the low-hydraulic-impedance grain

packing inside the hopper) should be a pressure node. On the other hand, one expects a maximum of the pressure oscillations at the bottom plug (there the displacement amplitudes should be minimal). The lowest-frequency resonance mode should then correspond to a length of the plugs–bubbles sequence equal to $\lambda_{osc}/4 = 1$ m. The actual length is of order 0.8 m, so the agreement is reasonable in view of the crudeness of the approximations involved.

In the low-frequency limit, the imaginary term in (26) which is partly responsible for the damping of the oscillations is found equal to $i\omega^3 K(c_p)\rho_g c_p/\eta$. It may be compared to the two other terms which are of the order of ω^2. The experimental values yield a ratio of the order of 0.1. This term therefore contributes significantly to the damping of the oscillations.

A second dissipative mechanism is wall friction. The ratio of the wall friction term $F_{wj}^1/\pi R^2$ in equation (22) and the acceleration term $\rho_g l_p \mathrm{d}q_j^1/\mathrm{d}t$ is of order

$$\frac{F_{wj}^1}{\pi \rho_g c_p R^2 l_p g}\frac{g}{\omega u^1} = \frac{F_{wj}^1}{\pi \rho_g c_p R^2 l_p g}\frac{g}{\omega^2 \delta z^1} :$$

the first factor corresponds to the ratio between the oscillating component of the friction force and the weight of the plugs, δz^1 is the typical amplitude of the plug oscillations and u^1 the corresponding velocity. For an amplitude of a few centimetres, the second factor is of order unity so that the ratio of the fluctuations of the friction force to the weight of the plugs characterizes the attenuation. In some cases, the instantaneous friction force (constant + oscillating components) is large enough to induce a complete blockage of the flow (Aider *et al.* 1999). A periodic stick-slip-like motion of the wave system is then observed and can be considered as a high-amplitude limit of the oscillating-wave regime.

7. Conclusion

In this paper, we have shown that the complex nature of the various granular flow regimes in a vertical tube can be analysed in detail experimentally by combining global measurements (air and grain flow rates, mean pressure gradients and average particle fractions) with local information such as spatio-temporal diagrams and local particle fraction variations. Combined with simple mass and momentum conservation equations, these measurements enable one to determine important parameters, difficult to measure directly experimentally, such as the wall friction or the permeation of air through dense regions. The experiments have been realized in a tube of small diameter which allows one to observe conveniently a variety of flow regimes. The same approach might however be applied to other flow geometries and flow regimes.

In the stationary free-fall regime, particles accelerate under gravity until their weight is balanced by friction forces with the air and with the walls; at the same time, the particle fraction decreases with distance to ensure mass conservation. Friction on the walls can be determined without further assumptions by comparing the particle fraction and the pressure gradient at positions where the terminal velocity has been reached (the wall friction is found to be of the order of 15% of the grain weight in our experimental set-up). The full pressure and particle fraction profiles and the flow distribution in the various parts of the system can then be determined quantitatively at given air and grain flow rates: this requires only this wall friction value and a simple model without adjustable parameters for the friction between air and the particles.

In the steady wave regime, the upper part of the flow is occupied by a sequence of plugs and bubbles moving down at a constant velocity: the weight of the plugs is mostly balanced by an adverse pression gradient and, for a smaller part, by friction of the grains on the tube walls. These friction forces represent only 10% of the weight of the grains for beads with a clean, smooth surface and up to 20–30% for rougher ones. In contrast with the free-fall case, pressure is higher inside than outside the tube and the bottom part of the tube is occupied by a long, compact plug where pressure decreases linearly towards atmospheric pressure at the outlet. Both the permeability of the bottom plug and that of the moving ones must be sufficiently low to limit the downflow of air which, if it is too large, accelerates the motion of the waves and leads to their disintegration. Overall, and particularly when wall friction is low, density waves appear as the superposition of a global drift of the plug–bubble sequence and of a relative flow of grains with respect to the plugs of characteristics nearly independent of the global flow.

Combining measurements of the grain and air flow rates with spatio-temporal diagrams and particle fraction and pressure profiles allowed an estimation of particle and gas velocities in the various regions of the flow. Other parameters difficult to measure directly, such as the permeability of the moving or bottom plugs and the wall friction, could also be determined by using these measurements as inputs for simple mass and momentum conservation equations. In simple cases, the full pressure and particle fraction profiles could be determined through simple additional hypotheses. A similar approach was used in a simple case of unsteady flow (the oscillating-wave regime) to predict the characteristic oscillation frequency.

Several problems remain to be solved, however, before a full understanding of these flows is achieved. First, a theory predicting quantitatively the lengths of the plugs and the bubbles still needs to be established (the size of the moving plugs seems to be related mainly to the tube diameter). Second, we assumed throughout the paper that the concentration and the velocity of particles is uniform across the flow section. Significant three-dimensional effects are however to be expected in some cases: for instance grains might tend to concentrate in the centre of the tube inside the bubble regions which would induce a recirculation in the air flow. Indications of such effects have been observed on close-up video recordings of flows in the density-wave regime: grains seemed to concentrate on one side of the tube section inside the 'bubbles', which might be due to a residual tilt of the tube. Recent theoretical (Sinclair & Jackson 1989), Ocone, Sundaresan & Jackson 1993) and experimental (Srivastava *et al.* 1998) studies have analysed these segregation effects in vertical and inclined pipes: they predict significant variations of the particle concentration in the radial direction, even for vertical tubes. However, more information, particularly at the local scale, would be needed before attempting a quantitative comparison with these models. A third issue is the dependence of the flow regime on the grain shape and size and on the characteristics of their surface. Some preliminary re-sults reported in §5 have demonstrated the relevance of these properties. Finally, other flow regimes such as an intermittent compact flow also provide challenging questions.

REFERENCES

AIDER, J. L., SOMMIER, N., RAAFAT, T. & HULIN, J.-P. 1999 Experimental study of a granular flow in a vertical pipe: a spatio-temporal analysis. *Phys. Rev.* E. **59**, 778–786.

BEHRINGER, R. P. & JENKINS, J. T. (Eds.) 1997 *Proc. 3rd Intl Conf. on Powders and Grains*. A. A. Balkema.

CHEN, Y. M., RANGACHARI, S. & JACKSON, R. 1984 A theoretical and experimental investigation of flow in a vertical standpipe. *Ind. Engng Chem. Fundam.* **23**, 354–370.

DURAN, J. 1997 *Sables, Poudres et Grains*. Editions Eyrolles Sciences.

GINESTRA, J. C., RANGACHARI, S. & JACKSON, R. 1980 A one-dimensional theory of flow in a vertical standpipe. *Powder Techn.* **27**, 69–84.

JACKSON, R. 2000 *The Dynamics of Fluidized Particles*, Chap. 7. Cambridge University Press.

JAEGER, H. M. & NAGEL, S. R. 1992 Physics of the granular state. *Science* **255**, 1523–1531.

LEE, J. 1994 Density-waves in the flows of granular media. *Phys. Rev.* **49**, 281–298.

LEE, J. & LEIBIG, M. 1994 Density-waves in granular flow: a kinetic wave approach. *J. Phys.* I (Paris) **4**, 507–514.

LEIBIG, M. 1994 Pattern-formation characteristics of interacting kinematic waves. *Phys. Rev.* E **49**, 184–191.

LE PENNEC, T., AMMI, M., MESSAGER, J.-C., BIDEAU, D. & GARNIER, J. 1995 Effect of gravity on mass flow rate in an hour glass. *Powder Technol.* **85**, 279–281.

LE PENNEC, T., MÅLØY, K. J., FLEKKØY, E. G., MESSAGER J.-C. & AMMI, M. 1998 Silo hiccups: dynamic effects of dilatancy in granular flow. *Phys. Fluids* **10**, 3072–3079.

LE PENNEC, T., MÅLØY, K. J., HANSEN, A., AMMI, M., BIDEAU, D. & WU, X. L. 1996 Ticking hour glasses: experimental analysis of intermittent flow. *Phys. Rev.* E **53**, 2257–2264.

LEUNG, L. S. & JONES, P. J. 1978 Flow of gas–solid mixtures in standpipes, a review. *Powder Technol.* **20**, 145–160.

LIGHTHILL, M. J. & WHITHAM, G. B. 1955 On kinematic waves: I. Flood movement in long rivers, II. A theory of traffic flow on long crowded roads. *Proc. R. Soc. Lond.* A **229**, 281–316 and 317–345.

MOUNTZIARIS, T. J. & R. JACKSON, R. 1990 The effects of aeration on the gravity flow of particles and gas in vertical standpipes. *Chem. Engng Sci.* **46**, 381–407.

MUSHA, T. & HIGUICHI, H. 1976 The $(1/f)$ fluctuation of a traffic current on an express way, *Japan J. Appl. Phys.* **15**, 1271.

NOTT, P. & JACKSON, R. 1992 Frictional-collisional equations of motion for granular materials and their application to flow in aerated chutes, *J. Fluid Mech.* **241**, 125–144.

OCONE, R., SUNDARESAN, S. & JACKSON, R. 1993 Gas–particle flow in a duct of arbitrary inclination with particle–particle interactions. *AIChE J.* **39**, 1261–1271.

OLSON, R. M. 1970 *Essential of Engineering Fluid Mechanics*, 2nd edn. London: International Textbook Co.

PENG, G. & HERRMANN, H. J. 1994 Density-waves of granular flow in a pipe using lattice-gas automata. *Phys. Rev.* E **49**, R1796–R1799.

PÖSCHEL, T. 1994 Recurrent clogging and density-waves in granular material flowing through a narrow pipe. *J. Phys.* I (Paris) **4**, 499–506.

RAAFAT, T., HULIN, J.-P. & HERRMANN, H. 1996 Density-waves in dry granular media falling through a vertical pipe. *Phys. Rev.* E **53**, 4345–4350.

REYDELLET G., RIOUAL, F. & CLEMENT, E. 2000 Granular hydrodynamics and density-wave regimes in a vertical chute experiment. *Europhys Lett.* **51**, 27–33.

RICHARDSON, S. F. & ZAKI, W. N. 1954 Sedimentation and fluidisation: Part I. *Trans. Inst. Chem. Engrs* **32**, 33–53.

SAVAGE, S. B. 1979 Gravity flow of cohesionless granular materials in chutes and channels, *J. Fluid Mech.* **92**, 53–96.

SINCLAIR J. L. & JACKSON R. 1989 Gas–particle flow in a vertical pipe with particle–particle interactions. *AIChE J.* **35**, 1472–1486.

SRIVASTAVA, A., AGRAWAL, K., SUNDARESAN, S., KARRI, S. B. R. & KNOWLTON, T. M. 1998 Dynamics of gas–particle flow in circulating fluidized beds. *Powder Technol.* **100**, 173–182.

WANG C. H., JACKSON R. & SUNDARESAN S. 1997 Instabilities of fully developed rapid flow of a granular material in a channel. *J. Fluid Mech.* **342**, 179–197.